



## Combustion kinetics of coal chars in oxygen-enriched environments

Jeffrey J. Murphy<sup>1</sup>, Christopher R. Shaddix\*

*Combustion Research Facility, Sandia National Laboratories, Livermore, CA 94550, USA*

Received 15 September 2004; received in revised form 5 July 2005; accepted 22 August 2005

Available online 16 November 2005

### Abstract

Oxygen-enhanced and oxygen-fired pulverized coal combustion is actively being investigated to achieve emission reductions and reductions in flue gas cleanup costs, as well as for coal-bed methane and enhanced oil recovery applications. To fully understand the results of pilot scale tests and to accurately predict scale-up performance through CFD modeling, accurate rate expressions are needed to describe coal char combustion under these unconventional combustion conditions. In the work reported here, the combustion rates of two pulverized coal chars have been measured in both conventional and oxygen-enriched atmospheres. A combustion-driven entrained flow reactor equipped with an optical particle-sizing pyrometry diagnostic and a rapid-quench sampling probe has been used for this investigation. Highvale subbituminous coal and a high-volatile eastern United States bituminous coal have been investigated, over oxygen concentrations ranging from 6 to 36 mol% and gas temperatures of 1320–1800 K. The results from these experiments demonstrate that pulverized coal char particles burn under increasing kinetic control in elevated oxygen environments, despite their higher burning rates in these environments. Empirical fits to the data have been successfully performed over the entire range of oxygen concentrations using a single-film oxidation model. Both a simple  $n$ th-order Arrhenius expression and an  $n$ th-order Langmuir–Hinshelwood kinetic equation provide good fits to the data. Local fits of the  $n$ th-order Arrhenius expression to the oxygen-enriched and oxygen-depleted data produce lower residuals in comparison to fits of the entire dataset. These fits demonstrate that the apparent reaction order varies from 0.1 under near-diffusion-limit oxygen-depleted conditions to 0.5 under oxygen-enriched conditions. Burnout predictions show good agreement with measurements. Predicted char particle temperatures tend to be low for combustion in oxygen-depleted environments.

© 2005 The Combustion Institute. Published by Elsevier Inc. All rights reserved.

**Keywords:** Coal, char; Combustion; Kinetics; Oxy-fuel; O<sub>2</sub> enriched

### 1. Introduction

Alternatives to the conventional air-blown, atmospheric-pressure pulverized-coal (pc) combustion furnace are being investigated to enhance energy efficiency, reduce greenhouse-gas and pollutant emissions, and minimize the size and capital cost of future coal-based powerplants. Coal gasification is receive-

\* Corresponding author. Fax: +1 925 294 2276.

E-mail address: [crshadd@sandia.gov](mailto:crshadd@sandia.gov) (C.R. Shaddix).

<sup>1</sup> Current address: The Aerospace Corporation, P.O. Box 92957, Los Angeles, CA 90009, USA.

ing significant attention, both when integrated into a combined-cycle gas turbine powerplant (to form an integrated gasification combined-cycle, or IGCC, system) and when coupled to a synfuel chemical processing plant to produce liquid automotive fuel or hydrogen. Pressurized combustion of coal is also being explored, especially in the form of pressurized fluidized bed combustor (PFBC) technology. However, one of the most promising near-term alternatives to conventional pc combustion is atmospheric-pressure pc combustion in mixtures of oxygen and recirculated flue gas. This technology could be employed in new, smaller, stand-alone powerplants, but it is especially attractive as a potential retrofit technology for existing pc units. The CO<sub>2</sub>-rich product gas from this process can be beneficially used for enhanced oil recovery or coal-bed methane applications [1] or can be sequestered in geologic reservoirs. This combustion method utilizes enhanced oxygen levels (typically 28–30 mol%) to maintain a suitable furnace exit gas temperature (at high temperatures the molar specific heat of CO<sub>2</sub> is approximately 67% larger than that of N<sub>2</sub>) and sufficient heat-transfer rates to steam tubes.

For all of the above-noted technologies, a portion of the coal char conversion can be expected to occur in a high-temperature environment with the partial pressure of oxygen exceeding 0.21 atm. This is even true for coal gasification, whether air blown or oxygen blown, because significantly elevated pressures (typically 20–60 atm) are used in these processes. As a consequence of ongoing research and development of these coal conversion technologies, there is interest in understanding and measuring the combustion properties of coal under pressure and under oxygen-enriched (>21 mol% O<sub>2</sub>) conditions. Of course, for all of these processes some fraction of the char conversion occurs at intermediate to low partial pressures of oxygen, so the existing, extensive knowledge base of char combustion in reduced oxygen (<21 mol% O<sub>2</sub>) environments at atmospheric pressure is also relevant. Furthermore, two recent investigations of low-to intermediate-temperature char oxidation kinetics at elevated pressure [2–4] (using chars produced at 1 atm) have demonstrated that the intrinsic char oxidation kinetics are insensitive to the total pressure of the system, depending only on the partial pressure of oxygen. This result implies that char oxidation kinetic studies performed at a total pressure of 1 atm may be applied to the understanding of oxidation at elevated pressures, once proper accounting is made for differences in diffusion rates, boundary layer reactions, and char structure in the pressurized application.

Several previous studies have measured pulverized char particle temperatures and burnout times in high-temperature oxygen-enriched environments at

1 atm [5–9]. Similarly, simultaneous char particle size and temperature statistics [10–13] (and, in two cases, burnout times [11,13]) have been measured at various oxygen concentrations under pressurized conditions for pulverized coal particles. In addition, Tidona measured char particle temperatures and burnout times for laser-ignited pulverized coal particles surrounded by room temperature, high-O<sub>2</sub> fraction gas at 1 atm and under pressurized conditions [14]. Unfortunately, for all the studies using variable reactor pressures but one [10], the investigators did not use a common char source for the separate experiments, causing devolatilization-induced variations in the char properties to become convoluted with the fundamental oxidation process [15,16]. Furthermore, none of the previous investigations at elevated oxygen partial pressures derived coal char kinetic rate parameters from the measurements.

In the work reported here, an entrained flow reactor with an optical particle-sizing pyrometer is used to measure the joint temperature-size statistics of size-classified pulverized coal char particles burning at 1 atm both in conventional, reduced oxygen furnace conditions and in oxygen-enriched furnace conditions. From these data, we make the first quantitative determination of high-temperature pulverized coal char combustion rates in oxygen-enriched environments. In addition, char sampling and analysis also yield the first reported information on elemental release rates as a function of burnout in oxygen-enriched char combustion.

Deriving meaningful burning rate parameters from the measured temperature and size data is not trivial, especially over the wide range of gas compositions and particle temperatures considered in this investigation. Therefore, special care has been taken here to implement the best-available correlations for the high-temperature gas transport properties of gas mixtures. In addition, linear, nonlinear, and conventional ad hoc methods have all been fully explored in the current work for optimizing the fits of kinetic expressions to the data. Comparisons are made between particle burnout calculations using the recommended kinetic parameters and measured burnout. However, in contrast to previous work, the kinetic parameters are not adjusted to optimize the predicted burnout, because the large uncertainty in making burnout predictions does not justify an alteration of the kinetics derived from the optical measurements.

## 2. Experimental methods

The coal combustion experiments were performed in Sandia's optical entrained flow reactor facility, whose general design and operation have been previ-

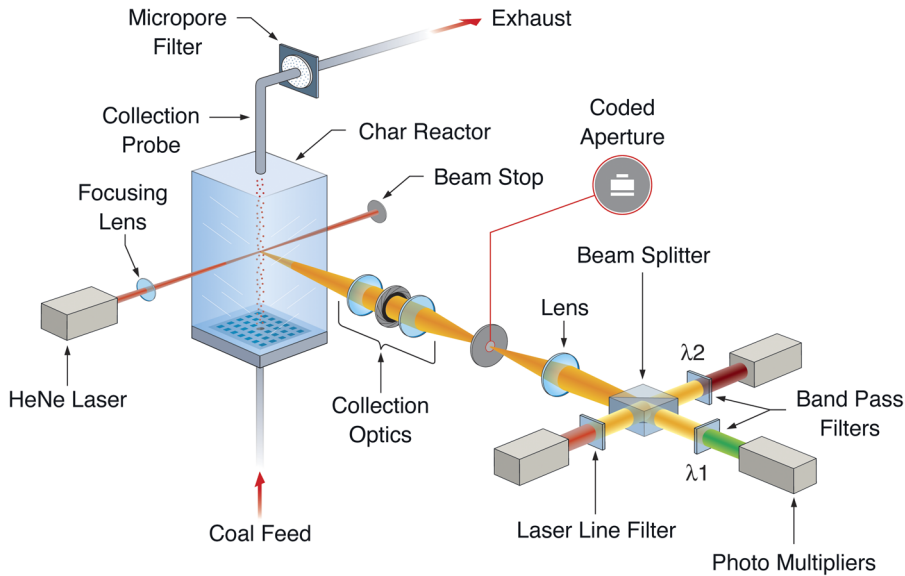


Fig. 1. Schematic diagram of Sandia's char kinetic entrained flow reactor, together with its particle-sizing pyrometer and char collection probe.

ously described in the literature [17,18]. A schematic of the facility is shown in Fig. 1. The furnace operates at 1 atm and uses a diffusion-flamelet-based Hencken burner to provide high-temperature gas that rapidly heats the injected coal particles and acts as the char oxidation medium. The use of pure gases to supply the Hencken burner allows a wide variety of product gas mixtures to be produced over a range of temperatures. In particular, oxygen concentrations approaching 50 mol% may be produced, using any one of a variety of diluents.

A particle-sizing pyrometer was used to simultaneously measure the velocity, diameter, and temperature of individual burning char particles at selected heights (i.e., residence times) within the reactor. A helium-quench, water-cooled sampling probe was used to collect char samples for chemical and physical characterization. The collection optics of the pyrometer project a particle image onto a coded aperture. Laser light scattered from the particles is used to trigger the data acquisition, ensuring that data are taken only if the particle image is in focus. Emission signals are detected through 40-nm FWHM bandpass filters with center wavelengths of 550 and 700 nm. The use of these filters avoids contamination of the pyrometry signals by line emission from sodium (589.0 and 589.6 nm) and potassium (766.5 and 769.9 nm). The size and velocity of the particle is calculated from the recorded 700-nm emission signal using the geometry of the coded aperture [17]. Temperature is calculated using a Wien's law ratio of both emission signals. The mean light (i.e., photon) intensity on the photomultiplier tubes was kept approxi-

mately the same for the widely varying combustion conditions through the use of calibrated neutral density filters.

The precision in these single-particle measurements was estimated using linearized versions of the equations used in the analysis, coupled with noise estimates from the recorded signal traces. Precision in the temperature measurements is better than  $\pm 1\%$  (typically  $\pm 20$  K), whereas the precision in the measured velocity is  $\pm 2\%$ . The particle size measurement has significantly lower precision, typically  $\pm 20\%$ .

Calibration of the pyrometer was performed over multiple temperature points using a high-temperature blackbody source (up to  $1700^\circ\text{C}$ ), focused onto a chopper wheel located along the furnace axis. Optical pinholes attached to the chopper wheel moved through the focal plane of the light collection optics, simulating emitting particles. This setup allowed a small correction (typically 5%) to be applied to the measured particle sizes, to account for the imperfect focus of the detection optics. A LabView data acquisition system was programmed to reject particle emission traces that indicate irregular particle trajectories or overlapping particle signals.

Furnace oxygen concentrations of 6, 12, 24, and 36 mol% were investigated with nitrogen as the diluent gas. Mixtures of hydrogen and ethylene were used as the burner fuel, resulting in a water vapor concentration of 14 mol% and a carbon dioxide concentration of 4 mol% in the furnace gases. Flow rates of fuel and oxidizer gases to the burner were chosen to maintain a common adiabatic flame temperature as the oxygen content in the burner exhaust was

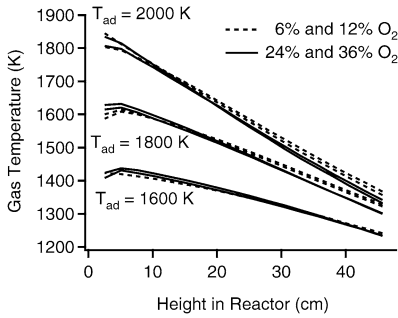


Fig. 2. Measured gas temperature profiles along the centerline of the combustion-driven furnace for the investigated char combustion conditions. Optical and physical sampling of char occurred over heights of 5–30 cm, with the maximum sampling height depending on the oxygen content of the flow.

varied, thereby providing a common gas temperature profile along the furnace centerline. Three different burner temperatures were investigated, in addition to the variation in oxygen concentrations, as shown in Fig. 2. These burner conditions correspond to adiabatic flame temperatures of 1600, 1800, and 2000 K. Gas temperatures along the centerline of the furnace were measured with a fine-wire (76  $\mu\text{m}$ ) type R beaded thermocouple and corrected for radiative loss [19]. The radiation corrections were calculated using the Collis and Williams correlation [20] for Nusselt number for cylindrical bodies and the best information available on wire emissivity and the transport properties of high-temperature gas mixtures [21]. Estimated uncertainty in the gas temperature measurement is  $\pm 50$  K. Unheated nitrogen carrier gas is used to convey the coal particles to the reactor, resulting in centerline temperatures at the base of the furnace that are well below the adiabatic flame temperature of the burner gases. Once the carrier gas has diffused into the surrounding burner gases (at a height of approximately 5 cm, which corresponds to the approximate height at which coal devolatilization ends), the centerline gas temperature steadily decreases with height in the furnace, on account of losses through the quartz walls. For each set of reactor conditions, there were 4 to 10 sampling positions, spaced 1.27 or 2.54 cm apart, at which optical data were taken. Typically, 200 particles were measured at each position. Char samples were collected and analyzed for a selected subset of these optical sampling positions.

When first operating the flow reactor under oxygen-enriched combustion conditions, the natural particle emission was found to be strong enough to trigger the data acquisition system in the absence of the laser-scattering trigger signal. These self-triggered particles may be out of focus (leading to overestimates of the particle size), and simply raising the

trigger threshold level to avoid self-triggering introduces a bias toward large particles. To overcome this difficulty, a higher-power 17 mW linearly polarized HeNe laser was incorporated to provide a stronger laser trigger signal, and a polarization filter was used in addition to the laser-line filter (1 nm FWHM) in front of the trigger detector to discriminate against natural particle emission.

Two characteristic North American coal sources were used for these experiments, in collaboration with investigations occurring at the CANMET Energy Technology Centre on oxygen-enriched and  $\text{O}_2/\text{CO}_2$  recycle coal combustion [22–24]. These coal sources are Highvale, a western subbituminous B coal that is extensively mined in Canada, and a commercial high-volatile eastern United States bituminous coal blend provided by Ontario Hydro, an electrical utility company. These coals were ground and sieved into a 106 to 125- $\mu\text{m}$  size fraction for use in Sandia's entrained flow reactor facility. The analyzed coal and ash properties of the ground and sieved coal are given in Table 1. The subbituminous coal has a higher content of volatiles, moisture, oxygen, calcium, and sodium, as would be expected. The subbituminous coal is a low-sulfur coal, whereas the eastern bituminous coal is a medium-sulfur coal. The proximate, ultimate, and ash analyses of the eastern bituminous coal are typical of a Pittsburgh seam coal [25], so it is presumed that this is the original source of the coal.

### 3. Numerical analysis

#### 3.1. Char burning rate

The instantaneous burning rate of an individual particle is determined from temperature, velocity, and size information by solving the energy balance for the particle, assuming a spherical, homogeneous, reacting particle surrounded by a chemically frozen boundary layer (i.e., single-film model). Heat losses from conduction and radiation are considered, as well as the effects of thermal inertia and Stefan flow [26]:

$$\frac{d_p \rho_p c_p v_p}{6} \frac{dT_p}{dz} = -\varepsilon \sigma (T_p^4 - T_w^4) - \frac{2\lambda}{d_p} \left[ \frac{\kappa/2}{e^{\kappa/2} - 1} \right] (T_p - T_g) + q \Delta h. \quad (1)$$

Here,  $q$  is the overall burning rate per unit external surface area of the particle. The quantity  $\kappa = (-q d_p / \lambda) \sum_i v_i c_{g,i}$  is a modified version of the Peclet number (i.e., the ratio of the convective velocity of the net mass leaving the particle surface to the diffusive velocity of heat leaving the surface). This quantity

Table 1  
Chemical analysis of coal samples

Proximate	Highvale		Eastern bituminous	
	(wt%, as rec'd)	(wt% dry)	(wt%, as rec'd)	(wt% dry)
Moisture	7.61		0.75	
Ash	11.39	12.33	8.82	8.89
Volatile	37.15	40.18	34.91	35.17
Fixed C	43.89	47.47	55.52	55.94
Ultimate	(wt% dry)	(wt% DAF <sup>a</sup> )	(wt% dry)	(wt% DAF)
C	60.70	69.23	77.33	84.87
H	4.01	4.57	5.08	5.57
O (by diff)	21.86	24.93	6.29	6.92
N	0.84	0.95	1.45	1.59
S	0.28	0.32	0.96	1.05
Higher heating value	(as rec'd)	(DAF)	(as rec'd)	(DAF)
MJ/kg	21.59	26.65	32.13	35.53
Btu/lb	9283	11,460	13,815	15,277
Ash analysis	(wt% of ash)		(wt% of ash)	
SiO <sub>2</sub>	48.29		54.11	
Al <sub>2</sub> O <sub>3</sub>	21.31		32.74	
Fe <sub>2</sub> O <sub>3</sub>	4.14		5.60	
TiO <sub>2</sub>	0.74		1.37	
P <sub>2</sub> O <sub>5</sub>	<0.10		0.08	
CaO	12.01		1.23	
MgO	1.09		0.73	
SO <sub>3</sub>	4.91		0.92	
Na <sub>2</sub> O	3.27		0.40	
K <sub>2</sub> O	0.25		2.31	
MnO	0.07		<0.01	

<sup>a</sup> Dry, ash-free.

characterizes the correction to the heat-transfer equation due to Stefan flow (see Ref. [26]). The  $\nu_i$ 's are analogous to stoichiometric coefficients  $\nu_{O_2} = OF$ ,  $\nu_{CO} = -2(1 - OF)$ , and  $\nu_{CO_2} = (1 - 2OF)$ , where  $OF$  is the oxidizer-to-fuel ratio, which is calculated from the CO<sub>2</sub>/CO production ratio at the char surface. The conduction term in Eq. (1) is written assuming a Nusselt number equal to 2, as is appropriate for a spherical particle surrounded by static flow. In fact, the particles in the flow reactor experience some velocity slip relative to the laminar gas flow, but this slip is estimated to be approximately 0.1 m/s, yielding a particle Reynolds number of less than  $10^{-6}$ . At this low Reynolds number, the assumption of both heat transfer and mass transfer occurring in a nonconvective flow environment appears justified.

It should be noted that there is concern in applying the single-film char combustion model for the combustion of particles larger than 100  $\mu\text{m}$  in oxygen-enriched atmospheres. Steady-state char boundary layer modeling by Mitchell et al. [27] suggested that significant CO conversion to CO<sub>2</sub> occurs in the boundary layer, with resultant impacts on particle temperature and burning rate, as the particle size

increases beyond 100  $\mu\text{m}$  and as gas and/or particle temperatures increase (e.g., for combustion in oxygen-enriched atmospheres). On the other hand, an analysis by Makino [28] suggests that the particle temperature and the bulk oxygen content have little influence on the critical diameter for CO flame ignition in the boundary layer.

The CO<sub>2</sub>/CO production ratio at the char particle surface is determined from the correlation CO<sub>2</sub>/CO =  $A_0 P_{O_2, s}^{\eta_0} \exp(-B_0/T_p)$  with the coefficients suggested by Tognotti et al. [29]:  $A_0 = 0.02$ ,  $B_0 = 3070$  K, and  $\eta_0 = 0.21$ . Then,  $OF = (1 + \psi)/2$ , where  $\psi = \text{CO}_2/\text{CO}/(1 + \text{CO}_2/\text{CO})$  is the fraction of carbon that becomes CO<sub>2</sub>. One could use semi-global intrinsic kinetics, such as the three-step model proposed by Hurt and Calo [30], to calculate the CO<sub>2</sub>/CO production ratio. However, these intrinsic kinetic approaches fit the rate parameters to reproduce correlations in the literature such as Arthur's [31] or Tognotti's [29], so there is no benefit to applying the intrinsic kinetic approach for this purpose.

The heat of reaction,  $\Delta h$ , is determined from the value of  $OF$  and by assuming that the char has the heating value of graphite. This assumption, previ-

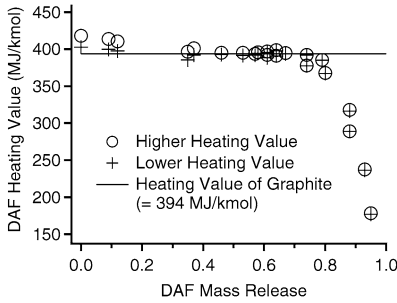


Fig. 3. Measured heating value of the eastern bituminous coal char as a function of the extent of coal mass burnt out in the entrained flow reactor. The heating value of graphite is shown as a line for comparison. The graphite heating value is based on the JANNAF heat of formation for  $\text{CO}_2$  ( $-394$  MJ/kmol) at standard conditions. Both the fractional coal mass release and the heating value are corrected to a dry, ash-free (DAF) basis.

ously untested to the authors' knowledge, was evaluated during this study by measuring the heating value of the eastern bituminous char that was collected over a wide range of burnout in the 12%  $\text{O}_2$ , intermediate temperature furnace environment. The results, shown in Fig. 3, indicate that the heating value of the devolatilized char (DAF mass release  $\geq 0.4$ ) is indeed the same as that of graphite. Surprisingly, the measured heating value of the char drops precipitously above 80% coal conversion. These high-conversion chars contain over 40 wt% ash, so it is presumed that the low apparent heating values for these chars result from either incomplete sample oxidation or some other error source in the calorimeter measurement. The commercial lab that performed the analysis did not see any unusual appearance in the final ashes and had insufficient sample to analyze for carbon in ash after the calorimetry measurement.

Gas properties were calculated using the expressions and molecular constants recommended by Mason and co-workers [32]. The recommendations of Paul and Warnatz [33] were used to calculate thermal conductivity. The transient heating rate of the particle,  $dT_p/dz$ , was approximated using the average particle temperature data collected in the experiments. The char particle density was assumed to be  $550$  kg/ $\text{m}^3$  for the eastern bituminous coal and  $700$  kg/ $\text{m}^3$  for the Highvale coal, consistent with mean measured values. A specific heat of  $2000$  J/kg K was used for the chars from both coals.

Because the  $\text{CO}_2/\text{CO}$  ratio depends on the partial pressure of oxygen at the char surface ( $p_{\text{O}_2,s}$ ), the gas-phase diffusion equation must be solved,

$$\frac{p_{\text{O}_2,s}}{p} = \gamma + \left( \frac{p_{\text{O}_2,\infty}}{p} - \gamma \right) \exp \left[ -\frac{q d_p}{2C D_{\text{O}_2,\text{mix}}} \right], \quad (2)$$

where  $\gamma = -(1 - OF)$  and  $C = P/RT_f$  is the average molar concentration of the gases in the boundary layer. Given a trial value of  $q$ , Eq. (2) must be solved iteratively because  $\gamma$  depends on the  $\text{CO}_2/\text{CO}$  ratio, which in turn depends on  $p_{\text{O}_2,s}$ . This solution is accomplished using a Newton–Raphson root-finding method, with  $p_{\text{O}_2,s}$  constrained to a range of zero to  $p_{\text{O}_2,0}$ . If the root-finding method strays from these bounds, or if convergence is not fast enough, a step is taken using bisection.

Given experimental measurements of particle size, temperature, and velocity, the burning rate is determined by iteratively solving Eq. (1) for  $q$  using the modified bisection algorithm described by Brent [34]. The solution method described in the preceding paragraph is used throughout the iteration to provide values of  $p_{\text{O}_2,s}$ , and thus  $\text{CO}_2/\text{CO}$  and  $\Delta h$ . This “nested” approach to solving the equations is more complicated than is required for calculating individual particle burning rates, but the additional complexity allows the same computer subroutines to be used with the nonlinear fitting techniques described later in this paper.

### 3.2. Char kinetic rate expressions

Historically, most kinetic data on burning coal char particles have been interpreted using an  $n$ th-order Arrhenius model of char combustion [25,35–37]. In this representation, the global reaction rate follows the expression

$$q = k_s(T_p) p_{\text{O}_2,s}^n, \quad (3)$$

where  $n$  is the reaction order,  $T_p$  is the particle temperature, and  $k_s$  is a temperature-dependent rate coefficient, assumed to follow an Arrhenius form:

$$k_s(T_p) = A \exp(-E/RT_p). \quad (4)$$

Another kinetic expression that has been periodically used to interpret char combustion kinetics is the Langmuir–Hinshelwood expression, which describes competing adsorption and desorption reactions on the char surface [38,39]. The most commonly applied form of this relation is the two-step Langmuir–Hinshelwood equation

$$q = \frac{k_2 k_1 p_{\text{O}_2,s}}{k_1 p_{\text{O}_2,s} + k_2} \quad (5)$$

with the  $k$ 's, as before, expressing Arrhenius dependence on the particle temperature.

As emphasized by Hurt and Calo [30], there are serious difficulties with both the  $n$ th-order Arrhenius (i.e., power law) and Langmuir–Hinshelwood relations for describing carbon oxidation over a range of temperatures and partial pressures of oxygen.

The Langmuir–Hinshelwood approach is theoretically more attractive than the  $n$ th-order Arrhenius approach because it provides a description of the O<sub>2</sub> adsorption, CO (and CO<sub>2</sub>) desorption process that is understood to be the general mechanism by which carbon is oxidized. However, the details of the adsorption/desorption chemistry are poorly understood, particularly for heterogeneous materials such as coal char. Furthermore, the two-step, single-site Langmuir–Hinshelwood kinetic expression that is most commonly used to describe char combustion predicts trends in pressure dependence as a function of temperature that run counter to a large number of measurements [30]. In fact, studies using thermogravimetric analyzers (TGAs) to measure the low- and intermediate-temperature oxidation of chars under both atmospheric pressure and pressurized conditions have found the  $n$ th-order Arrhenius expression to work well over a wide range of oxygen partial pressures [4,30,40]. On first appearance, this result is inconsistent with Langmuir–Hinshelwood kinetics. However, Hurt and Haynes [41] have shown that inclusion of heterogeneous reactivity distributions of reasonable width into Langmuir–Hinshelwood kinetics results in apparent power-law kinetic behavior over a wide range of Zone I oxidation conditions. In addition, experimental trends in intrinsic oxidation rates at low temperatures are well approximated when using the Hurt and Calo [30] three-step kinetic mechanism, including the reaction of molecular oxygen with the oxygen–carbon surface complex to produce CO<sub>2</sub> and an additional surface complex. At high temperatures, no existing kinetic approach can properly account for the low apparent reaction orders that have been consistently measured, albeit with lower quality data that spans a narrower range of variation of surface oxygen concentration than exists at low to intermediate temperatures.

### 3.3. Regression methodologies

In most previous studies of high-temperature char combustion kinetics, a given char kinetic expression was assumed to be applicable and a linear least-squares regression was performed on the data, or some subset thereof, to optimize the relevant kinetic constants. This procedure is complicated by Zone II particle combustion, where both the kinetic burning rate and the diffusion limitations are important, as is expected to be the case for the experiments reported here. Under these conditions, the diffusion rate of oxygen to the particle needs to be accounted for, as well as the mix of external surface reaction and internal pore reaction. Note that this latter difficulty does not, in fact, simply devolve into the classic Thiele kinetic analysis for reaction in homogeneous, porous

catalysts [42] (as usually assumed in the char combustion literature) unless the external surface reaction rate is negligible in comparison to the internal pore reaction rate. This point has been previously noted by Mitchell [43] and Fortsch et al. [44].

In principle, all three kinetic rate constants of the  $n$ th-order Arrhenius expression ( $A$ ,  $E$ , and  $n$ ) can be determined by using linear regression to fit the burning rate data directly to Eqs. (3) and (4) after applying a logarithmic transformation:

$$\ln q = \ln A - \frac{E_a}{RT} + n \ln p_{\text{O}_2, \text{s}} \quad (6)$$

In practice, this technique often results in a reaction order,  $n$ , close to zero, especially if the particles are burning near the diffusion limit. Because the classical Thiele analysis constrains the apparent, Zone II reaction order to lie between 0.5 and 1 [36,42], the traditional practice has been to assume a value of  $n$  (usually  $n = 0.5$ ) and then calculate  $k_s$  coefficients from the data. Then,  $A$  and  $E$  are determined by fitting a logarithmically linearized equation (4). With this approach, the use of a fractional oxygen exponent requires the elimination of any burning rates at or above the calculated diffusion limit.

Hurt and Mitchell [37] pioneered the derivation of accurate kinetic constants from single-particle optical data. When composing Arrhenius plots of  $k_s$  versus  $1/T_p$ , they noted that the single-particle rate coefficients cluster into groupings corresponding to “characteristic curves” of the equations governing gas-particle transport. The natural particle-to-particle variations in reactivity, as well as experimental noise, tend to scatter the data along these curves in a manner that biases the regression and the resulting kinetic constants, particularly when data are collected at only a few different conditions (three sample heights and two oxygen contents were investigated in their studies). To alleviate these difficulties, Hurt and Mitchell first removed all near-diffusion-limit datapoints from consideration and then defined a set of characteristic, synthetic data points for each measurement condition and calculated the burning rates for these synthetic datapoints. Finally, linear kinetic fits were performed (assuming a reaction order of 0.5) on these statistically representative burning rates.

Linear fitting techniques have a major difficulty when applied to Zone II char combustion: the elimination from the analysis of particles with measured burning rates at or above the calculated diffusion limit can significantly bias the result. Imagine a population of particles burning, on average, very close to the diffusion limit. Particle-to-particle variations in reactivity as well as experimental uncertainty will scatter the measured burning rates around the diffusion limit. Now, if all points at or above the diffusion limit are

eliminated from the analysis, the resulting population of points will, on average, be burning more slowly than the original population. In other words, the average particle reactivity derived from the analysis will be lower than the actual average reactivity of the original population. The fact that the determination of  $p_{O_2,s}$  is subject to significant uncertainty exacerbates this problem.

To provide a robust, quantitative means of comparing the fits of different char kinetics equations to the data measured in this study, a nonlinear regression technique was developed for determining the kinetics coefficients. The use of nonlinear techniques and genetic algorithms to determine Arrhenius kinetic constants has become increasingly common over the past decade [45–50], but to our knowledge has not been previously applied to char oxidation kinetics. In addition to avoiding the difficulties of linearized approaches for determining char kinetics near a limiting condition, such as the diffusion limit, nonlinear regression techniques allow one to readily incorporate a number of different kinetic expressions for fitting. In addition, the nonlinear regression technique yields quantitative confidence intervals that indicate the trust one can have in the parameter values that are derived from the technique.

To perform nonlinear regression, trial values of  $A$ ,  $E$ , and  $n$  are used to determine  $q$  and  $p_{O_2,s}$ , using Eq. (2) as described above. Rather than solving Eq. (1), however, we calculate a residual from Eq. (1) for each particle. A modified Levenberg–Marquardt method, based on the MINPACK routines LMDIF and LMDER, by Moré et al. [51], is used to optimize the values of  $A$ ,  $E$ , and  $n$  by minimizing the sum of the squares of the residuals. With this approach,  $q$  values are not actually determined as part of the optimization procedure, so there is no possibility of bias from characteristic curves as in the linear regression approach. Also, different expressions for the kinetic rate are simply applied as different functions from which to calculate  $q$ , given trial values of the relevant kinetic constants.  $A$  and  $E$  are constrained to be positive and  $n$  is limited to the range from zero to one using the transformations  $A = \exp\theta_0$ ,  $E = \exp\theta_1$ , and  $n = 1/(1 + \exp\theta_2)$ . Confidence intervals are calculated for each of the fitted kinetics constants using a linear approximation analogous to that used for linear regressions.

The technique described here has the advantage that it correctly handles particles that are in the diffusion limit, since the equations are valid throughout the range of conditions from the kinetic limit to the diffusion limit. If a regression is performed using a dataset containing particles that are all burning at or near the diffusion limit, the algorithm will return con-

fidence intervals covering the full range of parameter values (i.e.,  $0 \leq A \leq \infty$ ,  $0 \leq E \leq \infty$ , and  $0 \leq n \leq 1$ ).

Several different forms of the Langmuir–Hinshelwood two-step kinetic expression were considered in this study. The best performance was found for what we refer to as an  $n$ th-order Langmuir–Hinshelwood equation

$$q = \frac{k_2 k_1 p_{O_2,s}^n}{k_1 p_{O_2,s}^n + k_2}, \quad (7)$$

with the  $k$ 's, as before, expressing Arrhenius dependence on the particle temperature. One may think of this expression as a description of adsorption–desorption kinetics in which one does not specify the reaction order of the  $O_2$  adsorption step (as suggested in Ref. [52]). This form is also similar to, but not quite the same, as that which results from applying the conventional two-step Langmuir–Hinshelwood equation to Zone II combustion [44] and approximates the effective kinetic behavior for Langmuir–Hinshelwood kinetics when applied to char particles with a mildly heterogeneous reactivity distribution [41].

### 3.4. Char burnout model

To check the derived kinetic rates for consistency with the measured char burnout profiles, the equations describing particle mass and temperature were integrated in the reactor to obtain temperature and conversion profiles for each coal under intermediate-temperature conditions. The differential equation describing the evolution of particle mass is

$$\frac{dm_p}{dz} = \frac{\pi d_p^2 q W_c}{v_p}; \quad (8)$$

Eq. (1) describes the evolution of particle temperature.

The burnout model relies on numerous parameters, many of which have significant uncertainty. To determine how this parameter uncertainty affects the predictions of the burnout model, the input parameters and the output profiles are modeled as stochastic variables. The input parameters are each modeled using a normal distribution with a mean equal to the estimated value of the parameter and a standard deviation equal to half the estimated uncertainty in the variable. (Parameters with a lower bound, such as reaction rates, are modeled using a lognormal distribution.) The uncertainties in the input parameters are all assumed to be independent; thus, uncertainties in several input variables are modeled simultaneously using the same number of independent random variables. The output variables in the model are also stochastic variables. To study how uncertainty propagates through the model, a number of simulations are run

Table 2

Parameters used in the char burnout model, with estimated values and uncertainties

Symbol	Parameter	Estimate	2 $\sigma$ (%)
$\rho_{p,i}$	Initial char density (kg/m <sup>3</sup> )	700.0 (hv)	11 (hv)
		550.0 (eb)	5 (eb)
$T_{p,i}$	Initial char temperature (K)	1900.0	10
$d_{p,i}$	Initial char diameter ( $\mu\text{m}$ )	115.0	10
$T_g(z)$	Gas temperature (K)	1300–1685	4
CO <sub>2</sub> /CO	Heterogeneous product ratio	$0.02\rho_{\text{O}_2,s}^{0.21}e^{3070\text{ K}/T_p}$	100 <sup>a</sup>
$\rho_{\text{O}_2}$	Bulk gas oxygen content (mol%)	12.0	2
$T_w$	Wall temperature (K)	500.0	40
$\rho_{\text{ash}}$	Ash particle density (kg/m <sup>3</sup> )	2250.0	18
$Y_{c,i}$	Initial char carbon content (mass%)	73.7	18

<sup>a</sup> Simulated using a lognormal distribution.

in which the input parameters are varied randomly. The effects of these variations on the output variables are analyzed. This technique is superior to traditional sensitivity analysis since it captures nonlinear effects and parameter interactions.

The stochastic variables in the model are parameterized using polynomial chaos expansions [53]. These expansions allow one to write a stochastic variable as a series of modes, similar to a Fourier series expansion. Terms in the polynomial chaos expansion act to skew or shift the distribution of the variable. The more terms that are included in the expansion, the more accurately the expansion is expected to represent the true distribution of the variable. The polynomial chaos expansion is used here because of its favorable convergence properties.

Values of nine model input parameters are shown in Table 2, along with estimated uncertainties. The uncertainties are given as 95% confidence intervals, or twice the standard deviation,  $\sigma$ , of the distribution. The distributions are sampled using Sandia's Latin Hypercube sampling program [54]. Latin Hypercube is a stratified sampling technique that is more efficient than pure random sampling and provides faster convergence.

## 4. Results and discussion

### 4.1. Flow reactor photographs and observations

Fig. 4 shows photographs of the Highvale coal particle combustion history for the intermediate-temperature condition of the entrained flow reactor. The same trends with oxygen content evident in these photographs were also apparent for the eastern bituminous coal. As the bulk oxygen concentration increases, devolatilization occurs more rapidly and incandescence from the burning char particles is visible lower in the reactor. The char particle combustion

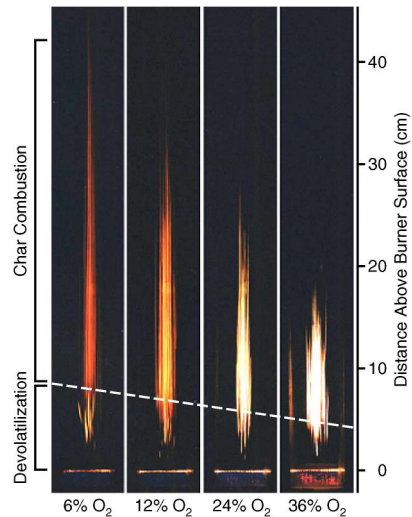


Fig. 4. Time lapse photographs of Highvale coal combustion in Sandia's entrained flow reactor under the intermediate gas temperature conditions. The oxygen content in the bulk gas is indicated below each photograph. The dashed line gives a qualitative indication of where coal devolatilization has ended and where char combustion is beginning. A length scale is indicated to the right of the photographs.

temperature increases (as evidenced by the incandescent intensity and color) as the oxygen concentration increases, and char burnout (evidenced by the endpoint of the incandescent particle traces) occurs much faster. It is also interesting to note that the bright luminous emission from oxidizing soot that is evident in the volatiles flames (low in the furnace) at low oxygen concentrations disappears at higher oxygen levels.

The apparent enhancement of the devolatilization rate with increasing oxygen content probably results from two factors: the closer proximity of the volatiles flame to the coal particle and the higher temperature of the volatiles flame. A closer proximity of

the volatiles flame at high oxygen levels is expected on the basis of diffusional constraints and the existence of the flame sheet at a standoff distance at which the emitted volatiles and the oxygen in the surrounding bulk gas diffuse toward each other in stoichiometric proportions [55]. Because soot inception is a relatively slow process in comparison to the small-molecule gas-phase reactions in the volatiles flame, the lack of observable soot thermal emission in the oxygen-enriched environments probably indicates that there is insufficient residence time for soot to form in the fuel-rich region between the particle and the surrounding volatiles flame. Adiabatic flame temperature calculations, using methane as a surrogate for the complex mixture of volatile gases evolved from the coal, show that the characteristic volatiles flame temperature in the entrained flow reactor environment increases from 2190 K at 6 mol% O<sub>2</sub> to 2450 K at 12 mol% O<sub>2</sub> to 2860 K at 36 mol% O<sub>2</sub>.

#### 4.2. Coal burnout and elemental release rates

Char collection was performed at the intermediate-temperature condition for each oxygen concentration at three different reactor heights for the Highvale coal and at five different heights for the eastern bituminous coal. These samples were submitted to ultimate and proximate analysis at a commercial analytical laboratory. The Highvale samples also underwent inductively coupled plasma (ICP) analysis of the content of the refractory metals Si, Al, and Ti. From these analyses, the fractional burnout of the two coals could be determined as a function of residence time in the reactor, and the fractional elemental release from the coal could be determined as a function of burnout. To estimate char burnout for the Highvale coal, individual refractory metal and total ash tracer techniques were examined. The different methods typically yielded values within a few percent of one another, with a small bias toward larger apparent burnout values when using titanium as the tracer. Because the burnout calculation assumes no loss of these metals and ash species through volatilization (and thus is really a lower limit to the actual burnout), the titanium-based burnout is assumed to be superior to use of the other analyzed metal species or the total ash content, and is used here. For the eastern bituminous coal, only information on the total ash content was available, so this was used as the tracer to determine the mass burnout.

Fig. 5 shows the burnout profiles of both coals at the intermediate-temperature condition as a function of the oxygen content of the flow. The residence time of the particles within the reactor has been calculated by applying a polynomial curve fit to the measured mean particle velocities as a function of

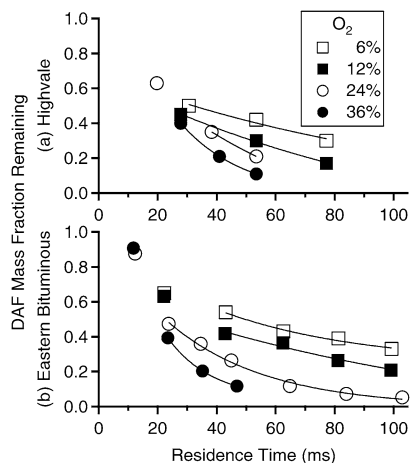


Fig. 5. Fractional coal mass remaining as a function of residence time in the entrained flow reactor, for different bulk oxygen concentrations and coal types, at the intermediate-temperature burner condition. Exponential curve fits to the data points are shown.

height in the reactor, extrapolating the fit back to the base of the furnace, and then integrating the inverse of the particle velocity over the reactor height. The use of higher oxygen concentrations clearly results in faster char burnout, as was also evident from direct visual observations and the time-lapse photographs of the coal combustion process. A few of the char samples, collected low in the reactor, have significant volatile contents and were evidently collected prior to complete coal devolatilization. From the trends in the burnout data, the high-temperature dry, ash-free (DAF) volatiles loss is approximately 50 wt% for the Highvale coal and 40 wt% for the eastern bituminous coal, consistent with existing databases for coals of this rank [56,57].

Fig. 6 shows the fractional elemental release of the two coals, as a function of coal burnout. Previous research under conventional combustion conditions has shown that the elemental release is a unique function of the total mass release when both are expressed on a DAF basis [25,58]. For Highvale coal, the trends of early hydrogen and oxygen release and delayed carbon, nitrogen, and sulfur release are in good agreement with the elemental release rates previously determined for subbituminous coals in the same entrained flow reactor [25]. Similarly, the nearly constant carbon release, faster hydrogen and oxygen release, and more uniform nitrogen and sulfur release of the high-volatile eastern bituminous coal are consistent with previous trends [25,58]. For both coals, there is no significant sensitivity of the DAF elemental release trends to combustion in 6% versus 36% O<sub>2</sub>, despite the substantial differences in particle temperature and burning rate over this range of conditions.

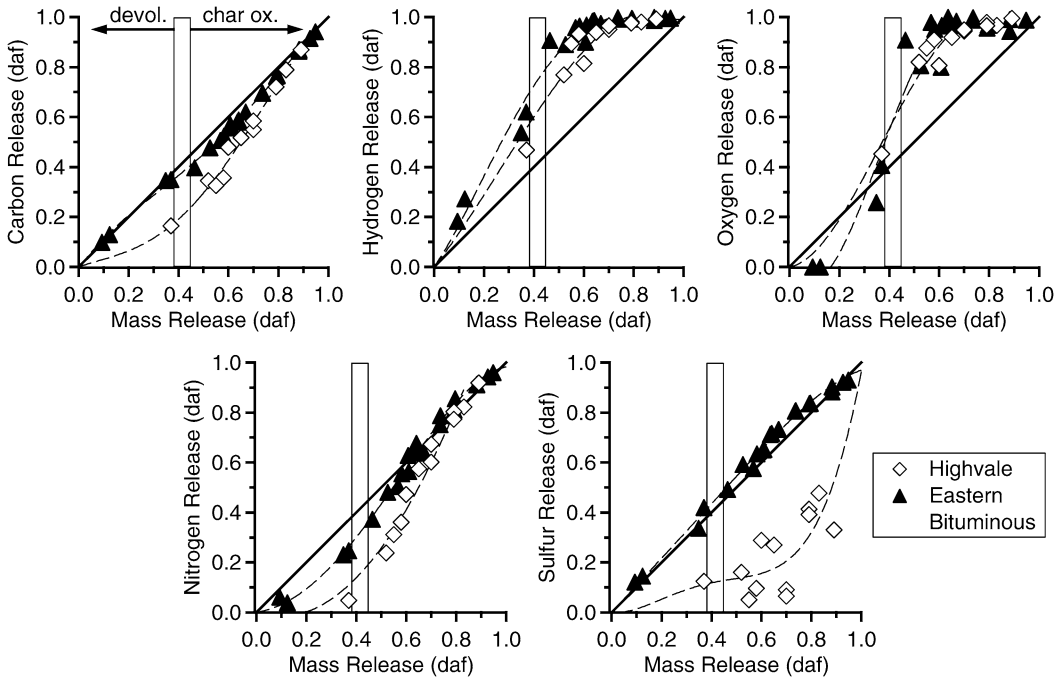


Fig. 6. DAF elemental release versus the DAF mass loss for combustion of Highvale subbituminous and high-volatile eastern bituminous coal in environments ranging from 6 to 36%  $O_2$ . The solid line indicates the unity relationship for elemental release equal to mass release. The vertical, rectangular box indicates the range of mass release corresponding to complete volatile loss for the two coals. The dashed lines represent simple polynomial curve fits to the experimental data.

The scattered data and slow apparent release of sulfur for Highvale coal probably reflect measurement difficulties associated with the large amount of sulfur associated with its ash.

#### 4.3. Measured temperature and size distributions

As has been previously observed in a number of studies, different char particles showed a significant variation in temperature at any given sampling height and burner condition, for any given coal. A portion of this variation may be attributed to actual differences in particle temperatures (resulting from the heterogeneous distribution of intrinsic reactivity, pore volume structure, and ash content within the particle population) and a portion results from measurement uncertainty. In Fig. 7, average measured char particle temperatures and diameters for the intermediate temperature flow condition are shown as a function of residence time in the flow reactor. The average particle temperatures for the Highvale coal are approximately 1800, 2000, 2200, and 2400 K at the 6, 12, 24, and 36% oxygen conditions, respectively. For the eastern bituminous coal, particle temperatures are slightly lower: 1800, 1950, 2100, and 2300 K for the same conditions. The average particle temperatures tend to increase at low residence times and then decrease at

high residence times for both coals under all conditions; the falloff with residence time is somewhat larger for the eastern bituminous coal.

For Highvale coal combustion in 6 and 12%  $O_2$  at the intermediate temperature condition, the actual distribution of char particle sizes as a function of burnout in the flow reactor was measured by Maloney et al. [59] and shows the expected decrease in mean char particle size (for near-diffusion-limit combustion) from 100  $\mu m$  for young chars down to 85  $\mu m$  for 40% char burnout. In contrast, the average char particle diameters measured with the in situ optical technique are larger than this and show an increase in particle size at short residence times, followed by a decrease in size at later times. The larger sizes measured in situ result from thermal expansion of the hot char and the inherent bias of the laser-triggered optical pyrometry technique to larger particles [13]. It should be noted that the distribution of in situ measured particle sizes is quite wide for either coal at any given measurement location, with standard deviations varying from 20 to 35  $\mu m$ . Therefore, the size distributions at all heights and flow conditions show substantial overlap, even for the Highvale coal burning in 36%  $O_2$ , in which the measured mean diameters are larger than for the other oxygen levels. Calculations show that the derived surface-specific particle burn-

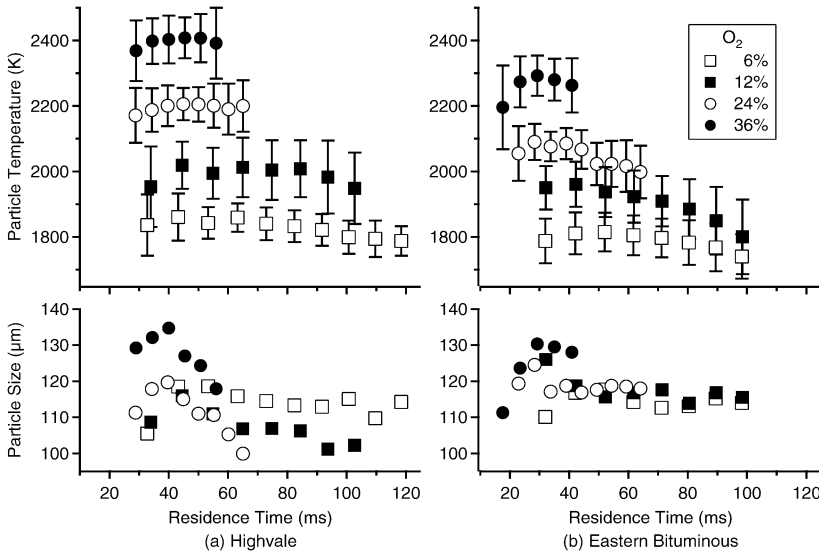


Fig. 7. Average measured char particle temperatures and sizes for the Highvale (a) and eastern bituminous (b) coals. The bars show the range of plus/minus one standard deviation of the measured temperature distribution around the average temperature.

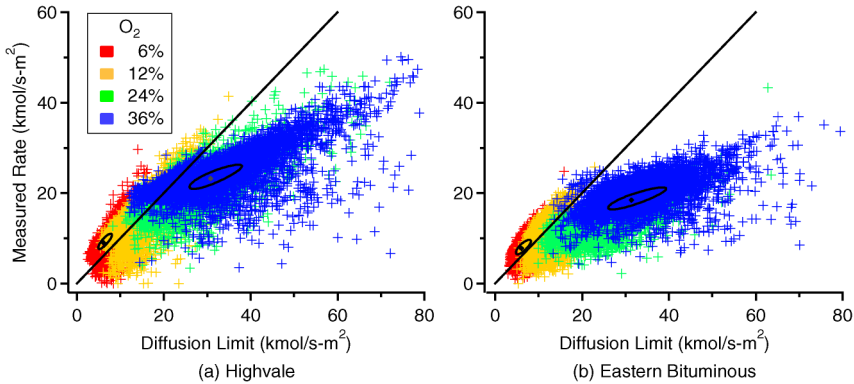


Fig. 8. Measured versus diffusion-limit burning rates for the Highvale (a) and eastern bituminous (b) coals. Points above the solid line have measured rates greater than the calculated diffusion-limit rate. The ellipses show 95% confidence regions for typical points.

ing rates are relatively insensitive to particle size in this size range (they are primarily dependent on particle temperature).

#### 4.4. Char burning rate trends

Fig. 8 shows the experimentally measured burning rates, for all three reactor temperature profiles, plotted against the diffusion-limit burning rates for both the Highvale and the eastern bituminous chars. The diffusion-limit burning rates are calculated by solving Eqs. (1) and (2) for both  $q$  and  $T_p$  using the measured particle sizes, while setting  $p_{O_2,s} = 0$ . The 95% confidence regions shown in these plots are typical for these data. The uncertainty in the diffusion-limit burning rate is much larger than that of the measured burn-

ing rate, because the diffusion-limit burning rate is inversely proportional to the particle diameter (which, as previously noted, has a high uncertainty).

The representation of the data shown in Fig. 8 is useful for confirming the accuracy of the boundary layer diffusion calculation and for evaluating the conditions under which the determination of meaningful kinetic rate information from the data may be possible. The good agreement that is evident between the calculated diffusion-limit burning rate and the measured burning rate as the bulk oxygen concentration approaches zero (forcing the char to Zone III combustion) provides direct evidence of the accuracy of the boundary layer diffusion calculation in this study. For combustion conditions in which the vast majority of data points straddle the diffusion limit, it is not possi-

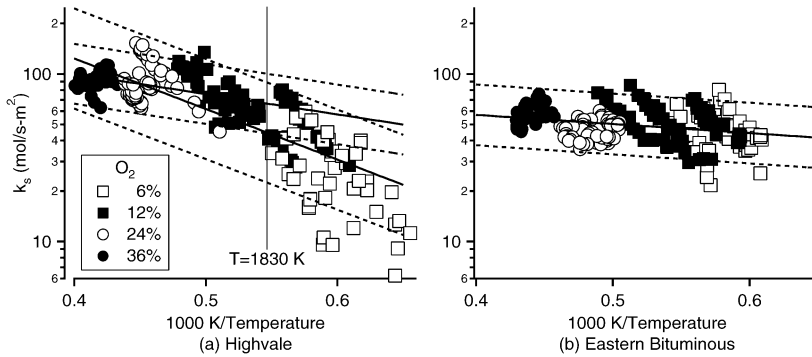


Fig. 9. Representative, median  $k_s$ 's and determination of the kinetic constants for the Highvale (a) and the eastern bituminous (b) coals using the method of Hurt and Mitchell for  $n$ th-order Arrhenius kinetics with an assumed reaction order of 0.5. For the Highvale coal, fits are shown for the entire set of median points and for those points with particle temperatures greater than 1830 K. The dotted lines show the 95% confidence prediction regions for the fits.

Table 3

Linear regression results for the  $n$ th-order Arrhenius rate equation

Fit	$A$ (mol/s m <sup>2</sup> atm <sup><math>n</math></sup> )	$E$ (kJ/mol)	$n$	Residuals <sup>a</sup>
<i>Highvale coal</i>				
Free fit	1073 ± 48	73.0 ± 0.9	0.02 ± 0.01	47
Fixed $n$	1498 ± 120	53.4 ± 1.5	0.50	157
Hurt and Mitchell	1989 ± 639	57.7 ± 5.2	0.50	121
Hurt and Mitchell ( $T_p > 1830$ K)	306 ± 121	23.2 ± 7.0	0.50	43
<i>Eastern bituminous coal</i>				
Free fit	615 ± 22	63.8 ± 0.7	0.04 ± 0.01	38
Fixed $n$	238 ± 16	26.6 ± 1.1	0.50	132
Hurt and Mitchell	94 ± 26	10.4 ± 4.2	0.50	45

<sup>a</sup> Proportional to the sum of the squared fit residuals divided by degrees of freedom of the fit residuals.

ble to extract any kinetic information. Fig. 8 shows that many of the particles are burning at or above the calculated diffusion-limit rate for combustion at the lower oxygen concentrations, where most previous char kinetic studies have been performed. This tendency is particularly evident for the Highvale coal. These findings are consistent with earlier char kinetic studies in this same flow reactor under similar temperature conditions with 6 and 12% oxygen, in which kinetic rate information could not be extracted from the data for subbituminous coals [60]. The eastern bituminous coal, which is less reactive, has a smaller, but still significant, percentage of char particles burning in the diffusion limit at the 6 and 12% oxygen conditions.

It is also apparent from these plots that increasing oxygen concentration in the bulk gas moves the char particles away from the diffusion limit, despite the increased particle temperatures in oxygen-enriched atmospheres. This finding implies that the increase in the kinetic burning rate in the oxygen-enriched atmospheres fails to offset the increase in the diffusional flux of oxygen to the particle. This trend also suggests that better kinetics data can be gath-

ered by making measurements at high oxygen levels. The smooth overlap of the data from oxygen-enriched atmospheres with that from reduced oxygen atmospheres suggests that there is no dramatic change in the burning behavior of the char particles over the investigated range of conditions. However, as noted previously, the applicability of the single-film model to derive char burning rates becomes increasingly uncertain as the oxygen content in the bulk gas increases. Interestingly, the observed trend of burning rate decreasing relative to the diffusion limit at elevated oxygen levels is the opposite of what would be expected if, in fact, oxidation of carbon monoxide became significant in the char boundary layer as the oxygen level increased [28,61].

#### 4.5. Char kinetic rate

##### 4.5.1. Linear fits of $n$ th-order kinetics

Fig. 9 and Table 3 show the results of a linear least-squares regression of the char burning rate data for the Highvale and eastern bituminous coals, using the Hurt and Mitchell approach for fitting the  $n$ th-order Arrhenius expression with an assumed reaction order of 0.5.

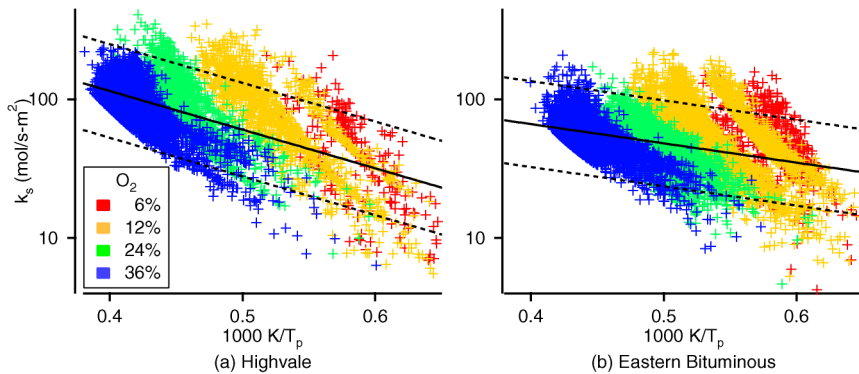


Fig. 10. Linear, least-squares fit of  $n$ th-order Arrhenius kinetics for the entire population of particle datapoints for the Highvale (a) and the eastern bituminous (b) coals, with an assumed reaction order of 0.5.

Two different Hurt and Mitchell fits are indicated for the Highvale coal, one that uses all of the median data points and one that selectively excludes those median points corresponding to measurement conditions that had a preponderance of data points in the diffusion limit (which includes all of the 6%  $O_2$  data and about half of the 12%  $O_2$  data). For those conditions, the median datapoints of the non-diffusion-limit particles are weakly reacting (probably corresponding to dense carbon or ash-dominated particles) and inappropriately bias the fit downward. If these low medians are removed from consideration (as has been the practice when applying this type of fit), the resultant Highvale coal fit shows a similar activation energy to that determined for the eastern bituminous coal and appropriately shows that the Highvale coal has a higher reactivity over the entire range of investigated temperatures. For both coals, the apparent activation energies determined by this linear fit are very low (23 kJ/mol for Highvale and 10 kJ/mol for the eastern bituminous coal). As will be shown later, the low activation energy results, in part, from forcing the kinetic fit to have a reaction order of 0.5.

A linear fit of the  $n$ th-order Arrhenius expression with an assumed reaction order of 0.5 to all the non-diffusion-limit particle kinetic data is shown in Fig. 10. The trending of the characteristic curves is clearly evident. Also evident is the dearth of non-diffusion-limit points at low particle temperatures (corresponding to combustion in 6 and 12%  $O_2$ ), particularly for the Highvale coal. As shown in Table 3, the kinetic constants determined by the linear fit of the individual particle data points are quite similar to those determined by the Hurt and Mitchell methodology. Indeed, the predicted  $k_s$  values are within 15% of one another over the particle temperature range of 1800–2500 K (encompassing almost all of the data).

If one performs a linear, free fit of the  $n$ th-order Arrhenius expression to all of the non-diffusion-limit data, the best-fit value for  $n$  is near zero, as shown

in Table 3. The best-fit activation energies, in this case, are around 70 kJ/mol, which is consistent with previous measurements of Zone II combustion kinetics [25,37]. A comparison of the relative fit residuals shows that the free fit is a much better representation of the data than the forced fit with an assumed reaction order of 0.5.

#### 4.5.2. Nonlinear fits of $n$ th-order kinetics

Table 4 shows the results of nonlinear fits of various kinetic expressions to the experimental data. The free fit of the  $n$ th-order Arrhenius expression to all of the data yields best-fit activation energies and reaction orders for both coals that are nominally equal, 45 kJ/mol and 0.18, respectively. By refitting the data with a common activation energy of 45.0 kJ/mol and a common reaction order of 0.175, the preexponentials may be compared to elucidate the relative reactivity of the coals. This analysis shows that, on average, the Highvale coal is 40% more reactive than the eastern bituminous coal. This finding is consistent with previous measurements of the char kinetic rates of subbituminous coals relative to Pittsburgh seam high-volatile bituminous coal [25,37].

Fig. 11 shows the results of a series of nonlinear fits to all of the experimental data of the  $n$ th-order Arrhenius expression for fixed values of  $n$ . The plot of residuals shows a distinct minimum for  $n = 0.17$ – $0.18$ . Also noteworthy is the dramatic decrease in the activation energy with increasing oxygen exponent, reaching zero for the Highvale coal for  $n \sim 1$ . The trends evident in Fig. 11 explain the observed difference in the kinetic fit constants for linear versus nonlinear fitting of the char burning rate data. With the exclusion of diffusion-limit data points in the linear fitting procedure, the fit becomes locally biased toward the unreactive portion of the particle population (as previously discussed), having a net effect of forcing the fit to a higher activation energy. As shown in Fig. 11, the best fit for a constraint of high activa-

Table 4

Nonlinear regression results for the  $n$ th-order Langmuir–Hinshelwood (LH) and  $n$ th-order Arrhenius rate equations

Fit	$A_1$ (mol/s m <sup>2</sup> atm <sup><math>n</math></sup> )	$E_1$ (kJ/mol)	$n$	$A_2$ (mol/s m <sup>2</sup> )	$E_2$ (kJ/mol)	Residuals <sup>a</sup>
<i>Highvale coal</i>						
Arrhenius	475 ± 30	45.9 ± 1.3	0.17 ± 0.01			421
Arrhenius, 24 + 36% O <sub>2</sub>	5230 ± 639	79.1 ± 2.1	0.46 ± 0.02			329
Arrhenius, 6 + 12% O <sub>2</sub>	4933 ± 939	83.2 ± 3.2	0.10 ± 0.03			258
LH	93 ± 26	0.1 ± <sup>-b</sup>	0.30 ± 0.04	26.2 ± 15.2	109.9 ± 7.5	400
LH, $n = 1$	2501 ± 1683	0.1 ± <sup>-b</sup>	1.00	1.1 ± 0.1	66.8 ± 2.3	453
LH-Essenhigh <sup>c</sup>	7617 ± 392	31.4	1.00	7.7 ± 0.1	100.0	566
<i>Eastern bituminous coal</i>						
Arrhenius	344 ± 16	45.5 ± 1.0	0.18 ± 0.01			265
Arrhenius, 24 + 36% O <sub>2</sub>	1086 ± 84	54.4 ± 1.3	0.50 ± 0.02			228
Arrhenius, 6 + 12% O <sub>2</sub>	1401 ± 227	69.1 ± 2.7	0.10 ± 0.02			168
LH	61 ± 17	0.5 ± <sup>-b</sup>	0.32 ± 0.04	20.0 ± 11.8	107.4 ± 7.3	260
LH, $n = 1$	1192 ± 742	0.0 ± <sup>-b</sup>	1.00	0.6 ± 0.1	60.7 ± 2.0	295
LH-Essenhigh <sup>c</sup>	2618 ± 97	31.4	1.00	8.1 ± 0.2	100.0	413

<sup>a</sup> Proportional to the sum of the squared fit residuals divided by degrees of freedom of the fit residuals.

<sup>b</sup> For these fits, the confidence interval for  $E_1$  was 0–∞.

<sup>c</sup> Activation energies taken from Ref. [39],  $E_1 = 31.4$  kJ/mol and  $E_2 = 100.0$  kJ/mol.

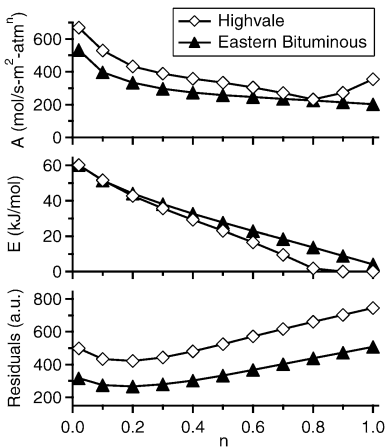


Fig. 11. Best-fit  $A$  and  $E$  and relative residuals for nonlinear fits of the  $n$ th-order Arrhenius model versus choice of  $n$ .

tion energy is a reaction order of zero, as evidenced in the linear fit results. Similarly, constraining the reaction order to be 0.5 forces the activation energy to be relatively low, as also seen in the linear fit results.

As shown in Table 4, nonlinear fits of the  $n$ th-order Arrhenius expression to only the oxygen-enriched data yield higher activation energies than are found for fits to the complete dataset (79 and 54 kJ/mol, vs 46 kJ/mol). In addition, the apparent reaction orders are considerably higher (0.5 vs 0.2). Because the oxygen-enriched combustion data do not contain many datapoints at or above the diffusion limit, an argument can be made to weight kinetic fits of these data over fits to the complete dataset, even when applying this to char combustion in conventional environments. In addition, the reaction order of 0.5 that is

found for the fit to the oxygen-enriched data is more compatible with the classic Thiele analysis, as previously discussed.

Table 4 also shows that nonlinear fits of the  $n$ th-order Arrhenius expression to the reduced oxygen data (6 and 12% O<sub>2</sub>) yield higher activation energies (83 and 69 kJ/mol) than are found for fits to the complete dataset. As mentioned previously, activation energies of 70–80 kJ/mol are consistent with past measurements of coal char kinetics in reduced oxygen atmospheres [25,37]. The best-fit reaction order for the reduced oxygen data is 0.1 for both coals, which explains why the fit to all of the data yields a reaction order that is significantly lower than the value of 0.5 determined for the oxygen-enriched combustion conditions.

#### 4.5.3. Nonlinear fits of Langmuir–Hinshelwood kinetics

Fig. 12 shows the results of a nonlinear free fit of the  $n$ th-order Langmuir–Hinshelwood expression to all of the experimental data. Because the char burning rates ( $q$ 's) that are being fit depend on both particle temperature and surface oxygen partial pressure, the results of the fit cannot be conveniently shown on an Arrhenius plot of  $q$  vs  $1/T_p$ . Instead, we resort to giving a comparison of the predicted versus the measured burning rate. The best-fit kinetic parameters, shown in Table 4, yield an activation energy for  $k_1$  (the step representing adsorption) of essentially zero and for  $k_2$  (representing desorption) of  $\sim 110$  kJ/mol. The best-fit reaction order for the adsorption step is 0.3, similar to the reaction order of 0.2 found for the nonlinear fit of the  $n$ th-order Arrhenius expression to all of the data. If the reaction order of the adsorption step is set

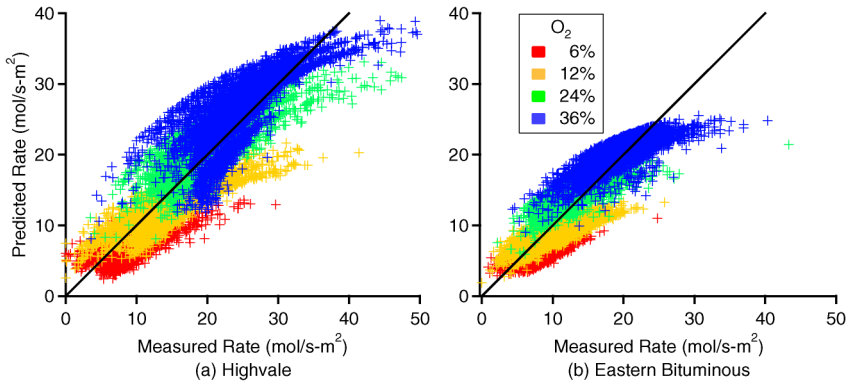


Fig. 12. Predicted versus measured burning rate for a nonlinear free fit of the  $n$ th-order Langmuir–Hinshelwood expression for Highvale (a) and eastern bituminous (b) coal chars.

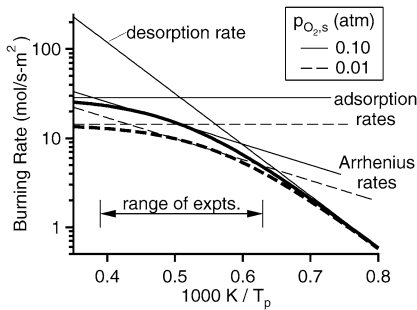


Fig. 13. Comparison of  $n$ th-order Langmuir–Hinshelwood equation to the  $n$ th-order Arrhenius expression for two different surface oxygen partial pressures, using best-fit coefficients for the eastern bituminous coal. The adsorption and desorption limits of the Langmuir–Hinshelwood expression are indicated, as are the  $n$ th-order Arrhenius rates and the range of experimentally measured particle temperatures.

to one, as in the traditional Langmuir–Hinshelwood equation, the activation energy for  $k_1$  is again forced to zero, the activation energy for  $k_2$  is reduced to 60–70 kJ/mol, and the residuals show that the fit is inferior to the fit when  $n$  is allowed to vary. If one goes further and adopts the activation energies proposed by Essenhigh and Mescher [39] for the adsorption and desorption steps, fitting just the preexponentials for the two kinetic rates, the quality of the fit deteriorates significantly.

Table 4 shows that the normalized residuals from the fit of the  $n$ th-order Langmuir–Hinshelwood equation are slightly lower than those from the  $n$ th-order Arrhenius fit to all of the data, indicating the Langmuir–Hinshelwood expression yields a superior fit. Fig. 13 gives a comparison of the best-fit  $n$ th-order Arrhenius expression and  $n$ th-order Langmuir–Hinshelwood equation for the eastern bituminous coal char, for two characteristic values of surface oxygen partial pressures. As is evident in the figure, the Langmuir–Hinshelwood fit has placed the exper-

imental data in the transition region (i.e., “roll-off”) between desorption control (at lower temperatures) and adsorption control (at higher temperatures). Thus, there is considerable curvature in the dependence of  $\log q$  on  $1/T_p$  in the temperature range of interest. The  $n$ th-order Arrhenius expression can provide only a linear dependence of  $\log q$  on  $1/T_p$ . The improved fit of the Langmuir–Hinshelwood relation indicates that the experimental data demonstrate some of this curvature, which may be important when extrapolating the fits to lower or higher temperatures than investigated here.

#### 4.6. Results of burnout calculations

Results of the burnout model calculations when using the best-fit  $n$ th-order Langmuir–Hinshelwood equation are shown in Fig. 14. These calculations were initiated at a residence time of 25 ms, when devolatilization is complete. The predictions generally show a good correlation with the measured dry, ash-free mass loss rate under the different combustion conditions, although the burnout rate of the Highvale coal under oxygen-enriched conditions is overestimated. Note that this model does not include mechanisms for ash inhibition, statistical kinetics, or thermal annealing of the char [62], so the burnout rate at high extents of conversion tends to be overestimated. Char particle temperatures are predicted well under oxygen-enriched combustion conditions, but tend to be underpredicted, particularly at long times, for reduced oxygen combustion conditions. This underprediction is caused, in part, by the inherent bias of the optical diagnostic measurement system to capturing data on larger particles (i.e., with this bias, the measured particle temperatures at long residence time correspond to larger initial particles than the 115  $\mu\text{m}$  assumed in the burnout calculation).

Samples of the calculated uncertainty in the burnout profiles are shown in Fig. 15. To calculate the

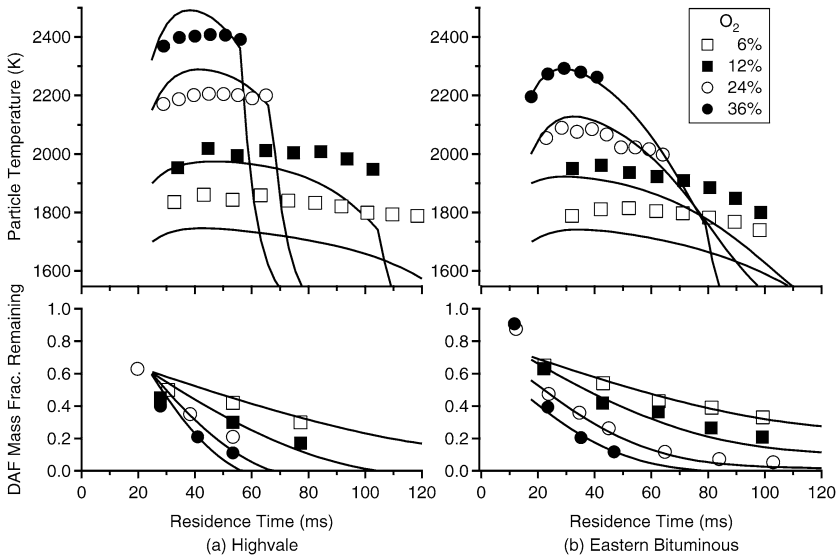


Fig. 14. Results of burnout model simulations for the Highvale (a) and the eastern bituminous (b) coals, using the best-fit kinetic parameters for the  $n$ th-order Langmuir–Hinshelwood equation.

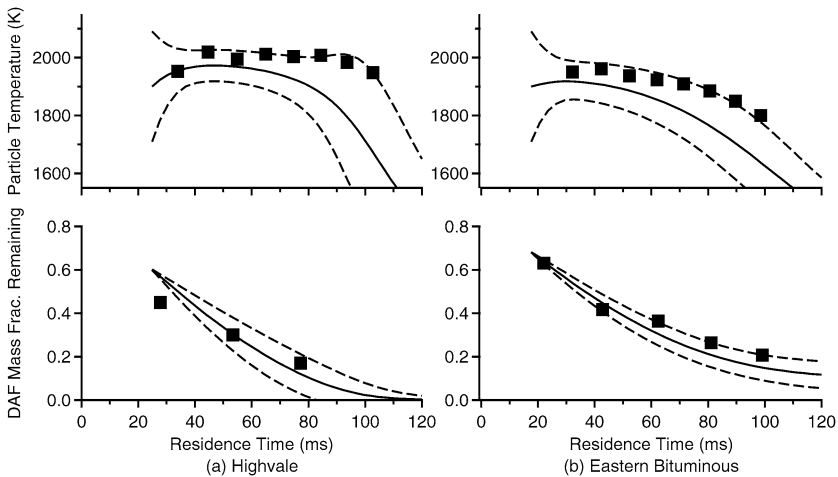


Fig. 15. Burnout model simulations for the Highvale (a) and the eastern bituminous (b) coals for combustion in 12%  $O_2$ . The nominal burnout model result is shown as a solid line, and dashed lines indicate the 95% confidence limits for the simulation, based on the parameter uncertainties given in Table 2.

uncertainty, all nine parameters shown in Table 2 were varied simultaneously over 24,000 simulations. Several runs were done with different random number seeds to check for convergence. The devolatilization mass loss is assumed to be known for these simulations, so the uncertainty in char mass burnout necessarily increases with time, demonstrating a cumulative effect. For char particle temperature, the uncertainty initially decreases during the peak combustion period and then expands to large values as some simulated particles burn out while others

still actively burning. This effect is particularly dramatic for the Highvale coal, which is calculated to undergo complete combustion in the 120-ms time window.

Fig. 16 shows how uncertainties in the different burnout model parameters contribute to the uncertainty in the calculated profiles of char particle temperature and burnout. Uncertainties in the initial char density and initial particle size are the major contributors to the Highvale coal profiles and to the initial portion of the burnout of the eastern bituminous

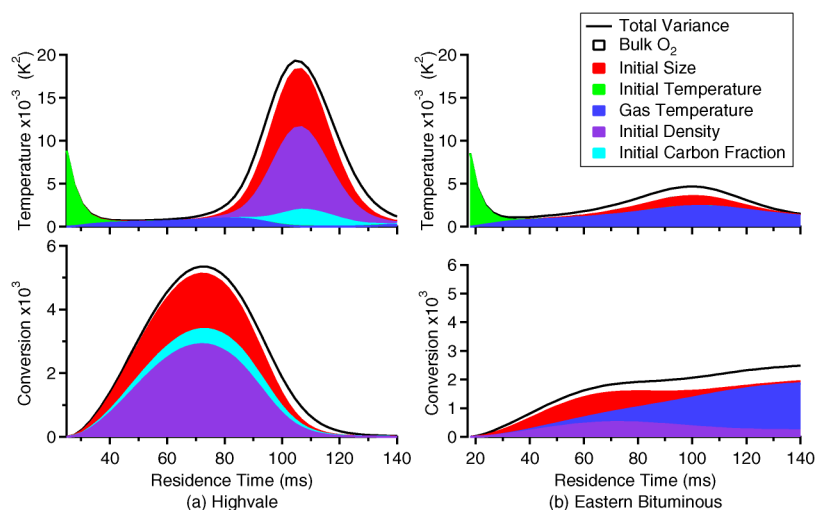


Fig. 16. Stacked plots of the contributing factors to the burnout model variance for the Highvale (a) and the eastern bituminous (b) coals for combustion in 12%  $O_2$ .

coal. Note that in this study the relative uncertainty in the initial char density of Highvale is over twice that of the eastern bituminous coal, which accounts for at least some of the difference in the impact of this factor on the simulation results. With the lower reactivity of the eastern bituminous coal, uncertainty in the gas temperature contributes significantly to the char temperature profile and to the latter portion of char burnout. Uncertainty in the bulk oxygen content also significantly influences the latter portion of char burnout of the eastern bituminous coal. Uncertainty in the initial particle temperature only contributes significantly to the char temperature profiles, and its effect rapidly becomes negligible as the particles heat up and begin to burn.

The burnout simulation results presented in Figs. 15 and 16 highlight the need to control and accurately measure all relevant coal, char, and combustion environment parameters when making comparisons between burnout simulations and experimentally measured particle temperatures and char burnout. In particular, a premium is placed on accurately knowing the apparent density of the char and the initial char particle size, as was recently emphasized in a related study [59].

## 5. Conclusions

The combustion reactivities of Highvale subbituminous coal char and an eastern United States high-volatile bituminous coal char were investigated in conventional and oxygen-enriched atmospheres using Sandia's optical entrained flow reactor. Oxygen-enriched combustion was found to significantly in-

crease the char combustion temperature and to reduce the char burnout time, as expected. The optical kinetic data, interpreted with a single-film oxidation model, demonstrate increasing kinetic control in enriched-oxygen combustion, despite the faster particle combustion rates. Both linear regression and nonlinear regression have been used to fit the optical kinetic data over the entire investigated range of oxygen concentrations, as well as subsets of that range. Fits with both a simple  $n$ th-order Arrhenius expression and an  $n$ th-order Langmuir–Hinshelwood expression were equally successful, yielding apparent reaction orders of 0.2 and 0.3, respectively, when applied over all of the data. Local fits of the  $n$ th-order Arrhenius expression to the conventional and oxygen-enriched atmospheres gave apparent reaction orders of 0.1 and 0.5, respectively. Char burnout rates and char particle temperatures are predicted reasonably well when applying a char burnout model with the derived kinetics.

## Acknowledgments

This work was supported by the U.S. Department of Energy through the National Energy Technology Laboratory's Power Systems Advanced Research Program, managed by Dr. Robert Romanosky. Mark Douglas, Eddy Chui, and Yewen Tan of CANMET provided the size-classified Highvale and Eastern Bituminous coal samples and arranged for chemical analysis of the collected Highvale char samples. Sandians Jimmy Ross and Gilbert Hofacker assisted in the operation of the entrained flow reactor and in char collection. Sandia is a multiprogram laboratory

operated by Sandia Corporation, a Lockheed Martin Company, for the United States Department of Energy under contract DE-AC04-94-AL85000.

## References

- [1] R. Payne, S.L. Chen, A.M. Wolsky, W.F. Richter, *Combust. Sci. Technol.* 67 (1989) 1–16.
- [2] D.G. Roberts, D.J. Harris, *Energy Fuels* 14 (2000) 483–489.
- [3] D.G. Roberts, D.J. Harris, T.F. Wall, *Fuel* 79 (2000) 1997–1998.
- [4] W.C. Hecker, P.M. Madsen, M.R. Sherman, J.W. Allen, R.J. Sawaya, T.H. Fletcher, *Energy Fuels* 17 (2003) 427–432.
- [5] L.D. Timothy, A.F. Sarofim, J.M. Béer, *Proc. Combust. Inst.* 19 (1982) 1123–1130.
- [6] S. Niksa, R.E. Mitchell, K.R. Hencken, D.A. Tichenor, *Combust. Flame* 60 (1984) 183–193.
- [7] B.J. Waters, R.E. Mitchell, R.G. Squires, N.M. Laurendeau, *Proc. Combust. Inst.* 22 (1988) 17–27.
- [8] M. Saito, M. Sadakata, M. Sato, T. Soutome, H. Murata, Y. Ohno, *Combust. Flame* 87 (1991) 1–12.
- [9] B.R. Stanmore, Y.-C. Choi, R. Gadiou, O. Charon, P. Gilot, *Combust. Sci. Technol.* 159 (2000) 237–253.
- [10] C.R. Monson, G.J. Germane, A.U. Blackham, L.D. Smoot, *Combust. Flame* 100 (1995) 669–683.
- [11] J.J. Saastamoinen, M.J. Aho, J.P. Hämäläinen, R. Hernberg, T. Joutsenoja, *Energy Fuels* 10 (1996) 121–133.
- [12] T. Reichelt, T. Joutsenoja, H. Spliethoff, K.R.G. Hein, R. Hernberg, *Proc. Combust. Inst.* 27 (1998) 2925–2932.
- [13] T. Joutsenoja, J. Saastamoinen, M. Aho, R. Hernberg, *Energy Fuels* 13 (1999) 130–145.
- [14] R.J. Tidona, *Combust. Flame* 38 (1980) 335–337.
- [15] T.F. Wall, G.-S. Liu, H.-W. Wu, D.G. Roberts, K.E. Benfell, S. Gupta, J.A. Lucas, D.J. Harris, *Prog. Energy Combust. Sci.* 28 (2002) 405–433.
- [16] D.G. Roberts, D.J. Harris, T.F. Wall, *Energy Fuels* 17 (2003) 887–895.
- [17] D.A. Tichenor, R.E. Mitchell, K.R. Hencken, S. Niksa, *Proc. Combust. Inst.* 20 (1984) 1213–1221.
- [18] R.E. Mitchell, *Combust. Sci. Technol.* 53 (1987) 165–186.
- [19] C.R. Shaddix, *Proc. 33rd National Heat Transfer Conference, HTD99-282*, ASME, New York, 1999.
- [20] D.C. Collis, M.J. Williams, *J. Fluid Mech.* 6 (1959) 357–384.
- [21] P.H. Paul, J. Warnatz, *Proc. Combust. Inst.* 27 (1998) 495–504.
- [22] E. Croiset, K. Thambimuthu, A. Palmer, *Can. J. Chem. Eng.* 78 (2000) 402–407.
- [23] E. Croiset, K.V. Thambimuthu, *Fuel* 80 (2001) 2117–2121.
- [24] E.H. Chui, M.A. Douglas, Y. Tan, *Fuel* 82 (2003) 1201–1210.
- [25] R.E. Mitchell, R.H. Hurt, L.L. Baxter, D.R. Hardesty, *Compilation of Sandia coal char combustion data and kinetic analyses*, Report No. SAND92-8208, Sandia National Laboratories, 1992.
- [26] J.J. Murphy, C.R. Shaddix, *Effects of Stefan flow on heat transfer from reacting carbon particles*, Report No. SAND2002-8072, Sandia National Laboratories, December 2003.
- [27] R.E. Mitchell, R.J. Kee, P. Glarborg, M.E. Coltrin, *Proc. Combust. Inst.* 23 (1990) 1169–1176.
- [28] A. Makino, *Combust. Flame* 90 (1992) 143–154.
- [29] L. Tognotti, J.P. Longwell, A.F. Sarofim, *Proc. Combust. Inst.* 23 (1990) 1207–1213.
- [30] R.H. Hurt, J.M. Calo, *Combust. Flame* 125 (2001) 1138–1149.
- [31] J.R. Arthur, *Trans. Faraday Soc.* 7 (1951) 164–178.
- [32] J. Bzowski, J. Kestin, E.A. Mason, F.J. Uribe, *J. Phys. Chem. Ref. Data* 19 (5) (1990) 1179–1232.
- [33] P.H. Paul, J. Warnatz, *Proc. Combust. Inst.* 27 (1998) 495–504.
- [34] R.P. Brent, *Comput. J.* 14 (4) (1971) 422–425.
- [35] M.A. Field, D.W. Gill, B.B. Morgan, P.G.W. Hawksley, *Combustion of Pulverised Coal*, The British Coal Utilisation Research Association, Leatherhead, England, 1967.
- [36] M.F.R. Mulcahy, I.W. Smith, *Rev. Pure Appl. Chem.* 19 (1969) 81–108.
- [37] R.H. Hurt, R.E. Mitchell, *Proc. Combust. Inst.* 24 (1992) 1233–1241.
- [38] R.H. Essenhigh, *Energy Fuels* 5 (1991) 41–46.
- [39] R.H. Essenhigh, A.M. Mescher, *Proc. Combust. Inst.* 26 (1996) 3085–3094.
- [40] E.M. Suuberg, M. Wojtowicz, J.M. Calo, *Proc. Combust. Inst.* 22 (1988) 79–87.
- [41] R.H. Hurt, B.S. Haynes, *Proc. Combust. Inst.* 30 (2005) 2161–2168.
- [42] E.W. Thiele, *Ind. Eng. Chem.* 31 (1939) 916–920.
- [43] R.E. Mitchell, *Proc. Combust. Inst.* 28 (2000) 2261–2270.
- [44] D. Fortsch, R.H. Essenhigh, U. Schnell, K.R.G. Hein, *Energy Fuels* 17 (2003) 901–906.
- [45] N.H. Chen, R. Aris, *AIChE J.* 38 (4) (1992) 626–628.
- [46] V. Cerda, A. Cladera, J.M. Estela, *Quím. Anal.* 15 (1996) 341–350.
- [47] N. Brauner, M. Shacham, *Chem. Eng. Process.* 36 (1997) 243–249.
- [48] T.Y. Park, G.F. Froment, *Comput. Chem. Eng.* 22 (1998) S103–S110.
- [49] S.P. Asprey, Y. Naka, *J. Chem. Eng. Jpn.* 32 (1999) 328–337.
- [50] L. Elliott, D.B. Ingham, A.G. Kyne, N.S. Mera, M. Pourkashanian, C.W. Wilson, *Combust. Sci. Technol.* 175 (2003) 619–648.
- [51] J.J. Moré, B.S. Garbow, K.E. Hillstrom, *User guide for MINPACK-1*, Report No. ANL-80-74, Argonne National Laboratories, 1980.
- [52] E. Croiset, C. Mallet, J.-P. Rouan, J.-R. Richard, *Proc. Combust. Inst.* 26 (1996) 3095–3102.
- [53] R.G. Ghanem, P.D. Spanos, *Stochastic Finite Elements: A Spectral Approach*, Springer-Verlag, New York, 1991.
- [54] G.D. Wyss, K.H. Jorgensen, *A user's guide to LHS: Sandia's Latin Hypercube Sampling software*, Report No. SAND98-0210, Sandia National Laboratories, 1998.

- [55] I. Glassman, *Combustion*, third ed., Academic Press, San Diego, CA, 1996.
- [56] S. Niksa, *Energy Fuels* 5 (1991) 673–683.
- [57] T.H. Fletcher, D.R. Hardesty, *Compilation of Sandia coal devolatilization data*, Report No. SAND92-8209, Sandia National Laboratories, 1992.
- [58] L.L. Baxter, R.E. Mitchell, T.H. Fletcher, R.H. Hurt, *Energy Fuels* 10 (1996) 188–196.
- [59] D.J. Maloney, E.R. Monazam, K.H. Casleton, C.R. Shaddix, *Proc. Combust. Inst.* 30 (2005) 2197–2204.
- [60] R.H. Hurt, R.E. Mitchell, *Proc. Combust. Inst.* 24 (1992) 1243–1250.
- [61] A. Makino, C.K. Law, *Proc. Combust. Inst.* 21 (1986) 183–191.
- [62] R. Hurt, J.-K. Sun, M. Lunden, *Combust. Flame* 113 (1998) 181–197.